

# **JGR** Atmospheres



#### **RESEARCH ARTICLE**

10.1029/2024JD041925

#### **Key Points:**

- Strong aerosol scattering in the subcloud transition zone near-cloud base are contributed to both aerosol hygroscopic growth and cloud fragments
- The hygroscopic growth factor at the Southern Great Plains showed distinct seasonal differences, weak in summer due to organics from anthropogenic amissions
- The effect of cloud fragments is strongest in summer, accounting for about one third of the enhanced scattering in the subcloud-transition zone

#### **Supporting Information:**

Supporting Information may be found in the online version of this article.

#### Correspondence to:

Z. Li, zli@atmos.umd.edu

#### Citation:

Hu, R., Li, Z., & Su, T. (2025). Investigating aerosol hygroscopicity in the subcloud transition zone and at the surface in the Southern Great Plains. *Journal of Geophysical Research: Atmospheres*, 130, e2024JD041925. https://doi.org/10.1029/2024JD041925

Received 5 JUL 2024 Accepted 29 JUL 2025

#### **Author Contributions:**

Conceptualization: Zhanqing Li Formal analysis: Rong Hu Funding acquisition: Zhanqing Li Investigation: Rong Hu, Zhanqing Li, Tianning Su

**Methodology:** Rong Hu, Tianning Su **Project administration:** Zhanqing Li **Resources:** Zhanqing Li

Software: Rong Hu Supervision: Zhanqing Li Validation: Rong Hu Writing – original draft: Rong Hu

Writing – review & editing: Zhanqing Li,

Tianning Su

© 2025. The Author(s).

This is an open access article under the terms of the Creative Commons

Attribution License, which permits use, distribution and reproduction in any medium, provided the original work is properly cited.

# Investigating Aerosol Hygroscopicity in the Subcloud Transition Zone and at the Surface in the Southern Great Plains

Rong Hu<sup>1</sup>, Zhanqing Li<sup>2</sup>, and Tianning Su<sup>2</sup>

<sup>1</sup>Faculty of Geographical Science, Beijing Normal University, Beijing, PR. China, <sup>2</sup>ESSIC and Department of Atmospheric and Oceanic Science, University of Maryland, College Park, MD, USA

**Abstract** Aerosols beneath a cloud base, a subcloud transition zone (SCTZ), are key to understand both the aerosol-cloud interaction and aerosol-radiation interactions. Lidars have been the primary means of observing aerosols in the SCTZ by virtue of enhanced light scattered by aerosol particles. The enhanced light maybe caused by several factors: the aerosol swelling effect due to hygroscopicity under high relative humidity, cloud 3-dimensional (3D) effect, aerosol nucleation into cloud droplets, etc. While each factor and process has been known, their relative contributions are much poorly quantified. This study explores the hygroscopicity and optical properties of aerosols in the SCTZ and at ground level in the Southern Great Plains (SGP) region. Utilizing comprehensive observational data from the U.S. Department of Energy's Atmospheric Radiation Measurement at the Oklahoma SGP site, including ground-based aerosol measurements and Raman lidar profiles from April 2021 to April 2022, this study extensively analyzes the influence of aerosol hygroscopic growth and cloud fragments on aerosol optical properties. Distinct seasonal variations in aerosol hygroscopic characteristics are revealed. At the ground level, aerosols in autumn and winter exhibit stronger hygroscopicity due to a higher proportion of inorganic content than summer. In the SCTZ, aerosols during summer show enhanced backscatter due to strong cloud fragmentation effects, with numerous cloud fragments elevating hygroscopicity beyond that observed in autumn and winter. These insights are crucial for understanding the interactions between aerosols at the surface and cloud layers, evaluating cloud condensation nuclei beneath clouds, and their implications for atmospheric radiation and climate modeling.

Plain Language Summary Light scattered by aerosols in the subcloud transition zone (SCTZ) is primarily influenced by aerosol hygroscopic growth and the presence of cloud fragments. Because this study uses vertically resolved Raman lidar profiles, the influence of 3D radiative effects is negligible (Várnai & Marshak, 2011, https://doi.org/10.1109/LGRS.2010.2049982). While the mechanisms of these effects have been well understood, their relative contributions remain poorly known and quantified. Using the measurements of hygroscopicity and optical properties of aerosols in the SCTZ in the Southern Great Plains region from April 2021 to April 2022, we investigated and quantified the influence of aerosol hygroscopic growth and cloud fragments on aerosol optical properties. Distinct seasonal variations in aerosol hygroscopic characteristics are revealed, stronger hygroscopicity in autumn and winter than in summer when enhanced backscatter is caused by cloud fragmentation elevating hygroscopicity beyond that observed in autumn and winter. The finding is important for understanding aerosol-cloud interactions and improving the estimation of cloud condensation nuclei.

#### 1. Introduction

Atmospheric aerosols, consisting of solid and liquid particles, experience a series of processes that impact both natural systems and mankind, such as formation (gas-to-particle conversion), aging, growth, removal, and transport (Jacobson et al., 2000; Pöschl, 2005; Prather et al., 2008). These processes render considerable spatiotemporal variabilities in their optical and hygroscopic properties to alter Earth's energy and water cycles (IPCC, 2013, 2021). As aerosols absorb ambient water vapor, they undergo changes in size, mass, shape, density, and refractive index, which in turn affect their impact on radiative forcing, cloud, and microphysics (Hänel, 1976; Hegg et al., 1996; Li et al., 2017; Rosenfeld et al., 2008; Su et al., 2024; Titos et al., 2014). Studies have indicated that aerosol properties differ substantially between near-cloud and clear-sky environments, with potential implications for surface radiation and boundary layer heating rates (Marshak et al., 2021). These differences

HU ET AL. 1 of 18

highlight the critical importance of examining aerosol behavior across various environmental conditions to better understand their role in radiative and climate effects.

The twilight zone (TZ), an area extending from the cloud boundary to clear skies, is defined by high vapor density that promotes aerosol hygroscopic growth (Koren et al., 2007), This zone extends horizontally 10 km from the cloud boundary, covering 17% of the global area and 34% of cloud-free areas. At 30 km, it includes 30% of the global area and 60% of cloud-free areas, thus occupying a significant portion of the Earth's surface (Bar-Or et al., 2011; Twohy et al., 2009). The impact of the TZ can extend horizontally up to 11 km from the cloud, with over 90% of the attenuation of longwave and shortwave radiation confined to areas within 4 km of the cloud (Eytan et al., 2020). These factors underline the importance of studying the hygroscopic growth of aerosols in the TZ for understanding Earth's radiation and climate change.

Many studies of the TZ rely on satellite remote sensing. Jeong and Li (2010) explored the correlation between aerosol optical thickness, as detected using sun photometers, and cloud coverage, discovering that up to 25% of the variance in aerosol optical thickness is attributed to aerosol hygroscopic growth, although the impact of cloud processes remains unclear. Calbó et al. (2017) compared observations of clouds using pyranometers, multifilter rotating shadow band radiometers, and total sky imagers, noting that during 10% of the observation times, it was challenging to distinguish between clouds and aerosols. Even identical physical conditions could be classified differently as cloudy or cloud-free, depending on whether it was day or night (Spänkuch et al., 2022). Even more significant uncertainties exist in the modeled direct, total, and scattered irradiance arising from different treatments of the radiative processes in the TZ (Jahani et al., 2019, 2020).

Three primary factors drive radiative uncertainty in the TZ: (a) aerosol hygroscopic growth (Bar-Or et al., 2012), where high relative humidity (RH) induces changes in the physical and optical properties of aerosols, (b) illmonitored clouds (Kaufman et al., 2005), where instrument limitations or algorithmic biases affect the retrievals of aerosol optical properties, and (c) three-dimensional (3D) radiative effects (Gristey et al., 2020; Marshak et al., 2006; Wen et al., 2006) where multiple scatterings of sunlight significantly impact horizontally integrated variables near cloud edges. These 3D radiative effects, such as enhanced scattering from aerosols illuminated by scattered sunlight, are particularly important for horizontal gradients in the TZ (Várnai & Marshak, 2002, 2011; Yang et al., 2022).

While 3D radiative effects are known to influence aerosol retrievals near clouds by enhancing horizontal gradients due to photon diffusion (Gristey et al., 2020; Marshak et al., 2006), their impact on the vertical gradients in the subcloud transition zone (SCTZ) is generally less pronounced. The SCTZ is primarily governed by local processes, including aerosol hygroscopic growth and interactions with cloud fragments, which operate on a vertical scale below cloud bases (Koren et al., 2007; Marshak & Davis, 2025). Moreover, lidar instruments provide vertically resolved profiles that are not affected by 3D radiative effects or instrument blurring, thus particularly well suited for investigating vertical structures in the SCTZ (Várnai & Marshak, 2011). By emphasizing the SCTZ, this study shifts focus to the physical mechanisms driving vertical aerosol and cloud property gradients, providing unique insights into aerosol-cloud interactions within the vertical column.

Understanding aerosol-cloud interactions requires knowledge of the vertical aerosol profile, yet most observations occur at ground or sea level (Li et al., 2011; Liu & Li, 2018; Y. Wang et al., 2023). Despite previous efforts using lidar data to study aerosol properties, such as Eck et al. (2014), most studies estimating aerosol radiative forcing have predominantly focused on surface measurements, limiting our understanding of aerosol behavior throughout the vertical column, including the PBL top and the SCTZ (Kahn et al., 2023; Painemal et al., 2017; Su et al., 2024).

There have existed significant gaps in our knowledge and understanding of vertical aerosol profiling within the SCTZ, which may contribute to notable uncertainties in understanding aerosol-cloud and aerosol-radiation interactions, as well as their broader climate effects. Aerosol variations in the SCTZ directly influence surface radiation and boundary layer heating rates, affecting atmospheric stability and feedback processes that drive cloud formation and persistence. Observational studies indicate that near clouds, aerosol optical depth can nearly double without significant changes in the Ångström exponent, underscoring the heightened impact of humidity and aerosol mixing state near clouds (Marshak et al., 2021). Accurately characterizing aerosol properties in the SCTZ is crucial for inferring the cloud condensation nuclei (CCN) and for studying the direct and indirect effects of aerosols on climate.

HU ET AL. 2 of 18

# Journal of Geophysical Research: Atmospheres

This study leverages a comprehensive set of measurements from the Southern Great Plains (SGP) site, integrating ground-based observations with Raman lidar (RL) profiles to assess aerosol hygroscopicity from the ground level to SCTZ. By combining these data sources, we provide a more detailed and vertically resolved understanding of aerosol properties and their interactions with cloud fragments. This paper is organized as follows: Section 2 describes the observation site and instruments, and Section 3 outlines the methods. Section 4 discusses the findings, and Section 5 concludes the study.

#### 2. Instruments and Data

Data for this study were sourced exclusively from the SGP site in Oklahoma, USA (36.6°N, 97.5°W), which is part of the U.S. Department of Energy's Atmospheric Radiation Measurement (ARM) program. They include lidar data, in situ aerosol property measurements, and meteorological data from 28 April 2021 to 23 April 2022. Since the available ground-based observation period does not cover the spring season, springtime cases were excluded from the analysis to ensure consistency across seasons in the comparison of aerosol hygroscopic properties. The RL operates at the 355-nm wavelength (Ferrare et al., 2006; Newsom et al., 2022), using the feature detection and extinction (RL-FEX) retrieval algorithm to obtain aerosol extinction and backscattering vertical profiles (Thorsen & Fu, 2015; Thorsen et al., 2015; Wu et al., 2021). The time and vertical resolutions of the lidar data product, processed using the RL-FEX retrieval algorithm, were 2 min and 30 m, respectively. Additionally, radiosonde data were incorporated into the value-added product data set (Newsom et al., 2017). Thanks to the RL's ability to differentiate between particulate and molecular signals; it directly measures the lidar ratio, thus reducing uncertainties in aerosol extinction and scattering assessments (Balmes et al., 2021) and reducing uncertainties in aerosol extinction and scattering (Thorsen & Fu, 2015). Additionally, RL-derived temperature (T) and water vapor mixing ratio (w) profiles (Newsom & Sivaraman, 2018) had a time resolution of 10 min and an initial vertical resolution of 60 m, which were linearly interpolated to 30 m for uniformity in comparisons. RL also incorporates a polarizing beam splitter, facilitating the measurement of aerosol linear depolarization ratios (Newsom et al., 2022).

This study utilized several ground-based aerosol measurements made using (a) a hygroscopic tandem differential mobility analyzer (H-TDMA) that uses two DMAs and a humidification system to measure aerosol hygroscopic growth factors (GF) at specified particle diameters of 50, 100, 150, 200, and 250 nm under 85% RH conditions, with a standard time resolution of about 30 min (Uin, 2016) and (b) a scanning mobility particle sizer (SMPS), model 3936 (TSI Inc.), which records particle sizes from 10 to 500 nm (Singh & Kuang, 2024). We calculated aerosol mass concentrations by assuming an aerosol density of 1.4 g cm<sup>-3</sup> (Parworth et al., 2015) as the mean of various aerosol types and (c) the aerosol chemical speciation monitor (ACSM) that measures the mass concentration and chemical composition of nonrefractory submicron aerosol particles by heating them to 600°C. This enables real-time measurements of mass concentrations across a range of 40 nm–1 µm and captures the chemical profiles of organics, sulfate, nitrate, ammonium, and chloride, with a sensitivity threshold below 0.2 µg m<sup>-3</sup>. The system averages signals over 30 min (Watson, 2017). Meteorological variables, including wind speed at 10 m and temperature and RH at a 2-m height, were recorded every minute (Ritsche, 2011).

## 3. Methodology

#### 3.1. RH Retrieval

Profiles of RH can be calculated using w and T profiles measured by the RL. Combined with atmospheric pressure profiles derived using the hypsometric equation, the calculation is performed using the Tetens formula provided by Monteith and Unsworth (2013). The equations used for these calculations are shown in Formulas S1–S4 in Supporting Information S1.

To assess the accuracy of the algorithm, RH profiles within 0–1.5 km, both for the entire data set and exclusively nighttime data, were compared with concurrent radiosonde measurements, as shown in Figure S1 in Supporting Information S1. There were instances where the computed RH exceeded 100%, which were treated as invalid values. As depicted in Figure S1a in Supporting Information S1, a comparison revealed a sound agreement, with  $R^2$  of 0.69 for a total of 15,848 sets of data samples. Note that the data at RH > 75% are more dispersed but not significantly biased, which is attributed to systematic errors in the RL. When considering nighttime data only in Figure S1b in Supporting Information S1, the correlation improved, with  $R^2$  increasing to 0.72 and the number of

HU ET AL. 3 of 18

valid data points equal to 6,258. Furthermore, for RH > 75%, the comparison is closer to 1:1 line in Figure S1 in Supporting Information S1.

#### 3.2. Aerosol Optical Properties and Hygroscopicity

Hygroscopic growth leads to larger aerosol particle size, which in turn affects the scattering cross-sections and the backscatter coefficient ( $\beta$ ). In this section, we aim to explore these optical changes in terms of the aerosol optical hygroscopic enhancement factor,  $f_{\beta}(RH)$ , at the 355-nm wavelength. This factor allows us to investigate variations in aerosol hygroscopicity under different environmental conditions and better understand the impact of hygroscopic growth on aerosol optical properties. The enhancement factor  $f_{\beta}(RH)$  is defined as follows:

$$f_{\beta}(RH) = \frac{\beta(RH)}{\beta(RH_{ref})} \tag{1}$$

where  $\beta$ (RH) and  $\beta$ (RH<sub>ref</sub>) represent the aerosol backscatter coefficient at a specific RH value and at a reference RH value at 355 nm, respectively. Due to the discrete nature of hygroscopicity parameters derived from this method, subsequent analyses often use Hänel's (1976) and Kasten's (Fernández et al., 2015) parameterization methods to model a continuous trend of hygroscopicity changes as follows:

$$H\ddot{a}nel: f_{\beta}(RH, \lambda) = \left[\frac{1 - RH}{1 - RH_{ref}}\right]^{-\gamma}$$
(2)

Kasten: 
$$f_{\beta}(RH, \lambda) = a \left[ 1 - \frac{RH}{100} \right]^{-b}$$
 (3)

where  $\lambda$  refers to the wavelength of light used in the measurement, and  $\gamma$ , a, and b are empirical parameters, with  $\gamma$  and b indicating the hygroscopic intensity, where higher values correspond to stronger hygroscopicity.

Variations in  $RH_{ref}$  prevent direct comparisons of hygroscopic enhancement factors at specific RH levels. Consequently, leveraging enhancements to the single-parameter scheme (Sicard et al., 2022), the aerosol optical hygroscopic enhancement parameter allows comparison across a wider range of RH values. The improved method is outlined as follows:

$$f_{\text{ref}}(\text{RH}) = f_{\text{min}}(\text{RH}) \left( \frac{1 - \frac{\text{RH}_{\text{min}}}{100}}{1 - \frac{\text{RH}_{\text{ref}}}{100}} \right)^{-\gamma}$$
 (4)

where  $f_{\text{ref}}(RH)$  is the modified hygroscopic enhancement factor adjusted to  $RH_{\text{ref}}$ , and  $f_{\text{min}}(RH)$  represents the baseline hygroscopic enhancement factor measured at the minimum observed RH ( $RH_{\text{min}}$ ).

Furthermore, aerosol hygroscopicity is characterized by the GF and the hygroscopicity parameter ( $\kappa$ ), which quantifies the water uptake potential of aerosols. Higher  $\kappa$  values indicate stronger hygroscopicity, which impacts the scattering and absorption properties of aerosols. GF represents the rate of change in particle size due to hygroscopic growth, defined as the ratio of the hydrated to dry particle diameter at a specified RH as follows:

$$GF = \frac{D_w}{D_d} \tag{5}$$

where  $D_w$  is the hydrated aerosol diameter, and  $D_d$  is the dry aerosol diameter.

Research has consistently demonstrated that aerosol particle hygroscopicity correlates with the proportion of organic and inorganic salts they contain, although most organic compounds are typically nonhygroscopic. Consequently, the relative amounts of these inorganic salts significantly influence aerosol hygroscopicity (Gysel et al., 2007). Given that the ACSM quantifies the mass concentrations of nonrefractory organic matter and inorganic salts in aerosols (Reilly & Wood, 1969), this study calculated aerosol hygroscopicity parameters using

HU ET AL. 4 of 18

the chemical ion combination scheme. This approach excludes chloride with details of the calculations provided in Figures S5 and S6, Table S1 in Supporting Information S1.

#### 3.3. Selection of Below-Cloud Hygroscopic Growth Cases

In this study, data sets of cloud-covered cases were compiled, with time alignments completed for RL and radiosonde profiles, excluding periods of precipitation. The determination of cloud presence was based on the feature mask within the RLPROFFEX1THOR data set, as indicated in Figure S2 in Supporting Information S1 (Cromwell et al., 2023). The RLPROFFEX1THOR algorithm, as described by Thorsen et al. (2015) and Thorsen and Fu (2015), uses elastic and Raman-scattered signals from nitrogen molecules to compute scattering ratios and depolarization ratios. These range-dependent detection thresholds are then applied to classify aerosol, cloud (distinguishing between liquid and ice), and precipitation. To minimize false detections, the algorithm applies consistency checks across multiple ratios and adjusts parameters iteratively until convergence is reached (Thorsen et al., 2015).

However, small undetected cloud fragments may still pose challenges due to the sensitivity and resolution limitations inherent in the algorithm. As noted in Thorsen et al. (2015), the algorithm compares favorably with other ARM detection schemes for clouds below 5 km, but its agreement with CALIPSO becomes less consistent at low altitudes (~1 km), particularly at night. This is likely due to the reduced sensitivity of CALIPSO to boundary layer clouds, as also acknowledged by Thorsen et al. (2015) which reinforces the advantage of using ground-based RL for near-surface cloud detection. RLPROFFEX1THOR's high vertical resolution and the signal-to-noise ratio enable more accurate classification of shallow liquid clouds, making it particularly suitable for identifying boundaries in the SCTZ.

In contrast, thermodynamic methods like the lifting condensation level (LCL) estimate cloud base height under the idealized assumptions of adiabatic lifting, which may not hold over land due to influences such as advection and radiative effects, as noted by Su et al. (2022). While this study adopts a consistent RLPROFFEX1THOR-based cloud mask to minimize classification bias across cases, we recognize that uncertainties in cloud classification remain. Future work will explore sensitivity to alternative detection methods such as LCL and MPL-derived boundaries to constrain cloud edge placement in the SCTZ.

Following prior research (Tackett & Di Girolamo, 2009), the criteria for selecting profiles containing clouds were (a) no clouds below 0.5 km and (b) clouds present between 0.5 and 1.5 km. The rationale for these criteria is threefold: first, the blind zone of RL extends around 0.2–0.3 km; second, water vapor concentrations are abundant below 1.5 km (Ferrare et al., 2013); and finally, clouds between the range of 0.5–1.5 km are predominantly coupled clouds (Su et al., 2022). Detailed information about the analyzed cases, including observation dates, cloud base, and top heights, has been summarized in Table S2 in Supporting Information S1.

Profiles of potential temperature ( $\theta$ ) and w obtained using radiosondes verified whether the boundary layer was well mixed, as indicated by minimal gradients in these profiles. Atmospheric uniformity was confirmed if the rates of change in  $\theta$  and w with altitude were less than 2 K and 2 g kg<sup>-1</sup> per kilometer, respectively (Granados-Muñoz et al., 2015). Additionally, considering fluctuations in environmental RH, cases where both the  $\beta$  and RH increased with altitude were selected to focus on profiles where hygroscopic growth is evident. This method aims to better attribute variations in  $\beta$  to changes in RH and excludes cases with constant  $\beta$ , as they are not concerned with the hygroscopic effects (Bedoya-Velásquez et al., 2018). Although no sensitivity test was conducted, the RLPROFFEX1THOR cloud mask has been validated against CALIPSO and AERONET for clouds below 5 km (Thorsen et al., 2015), attesting to its validity for vertical analysis in this study.

#### 4. Results and Discussion

#### 4.1. Surface Meteorology and Aerosol Hygroscopicity

According to the MET data set from ARM (Kyrouac et al., 2023), as illustrated in Figure S3 and Table S3 in Supporting Information S1, the SGP site experienced high temperatures and humidity during summer and low temperatures with high humidity in autumn and winter. Seasonal variations in wind speed and direction are significant, with wind rose diagrams (Figure 1) indicating predominant southerly airflow during summer, particularly at speeds exceeding 5 m s $^{-1}$ . In contrast, northerly winds are more common during autumn and

HU ET AL. 5 of 18

.com/doi/10.1029/2024JD041925 by Zhanqing Li - University Of Maryland,

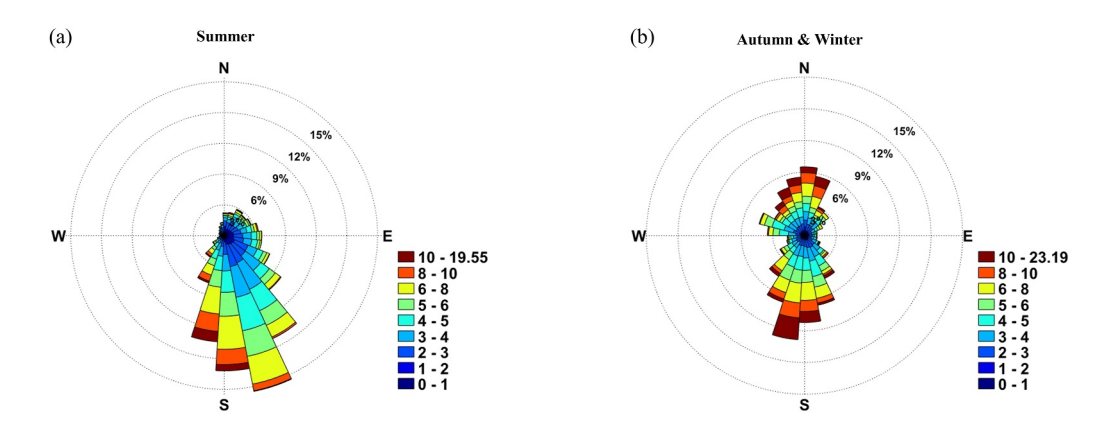


**Figure 1.** Wind speed and direction statistics for the Southern Great Plains of the United States. The percentage contours represent cumulative values across the data set, with warmer colors indicating higher wind speeds. (a) The summer wind rose diagram from June 2021 to August 2022 and (b) the autumn-winter wind rose diagram from October 2021 to February 2022.

winter, occurring with nearly two-thirds the frequency of southerly winds and more frequently at higher wind speeds.

Moreover, the SGP site's vicinity is influenced by surrounding agricultural emissions and coal combustion emissions from power plants (Liu et al., 2021; J. Wang et al., 2006), with densely populated urban areas to the south (Trishchenko et al., 2004). During summer, sulfate aerosols primarily from anthropogenic emissions predominate. In autumn and winter, biological emissions and wildfire outputs from the northern plains' grasslands and farmlands, combined with aerosol transport from the southeast, bring aerosols such as nitrates, leading to seasonal variations in aerosol types and hygroscopic properties.

Using the AOSHTDMA data set (Uin et al., 2021), the hygroscopic GF probability distribution (GF-PDF) of aerosols is analyzed at RH = 85% whose seasonal variation is shown in Figure 2. Summer results indicate that all GF-PDFs for five different particle sizes exhibit a unimodal distribution with narrow spectra and lower GF values, suggesting that summer aerosols are predominantly internally mixed with weaker hygroscopicity (Y. Wang et al., 2018). In contrast, during autumn and winter, the GF-PDF spectra broaden and GF values increase, particularly maintaining a unimodal distribution in the 50–150 nm nucleation mode aerosols, while the 250 nm accumulation mode aerosols exhibit a bimodal distribution. This reflects a higher degree of aging and stronger hygroscopicity in autumn and winter aerosols. Moreover, accumulation mode aerosols larger than 200 nm demonstrate external mixing characteristics, with the presence of hydrophobic black carbon likely causing lower hygroscopicity with GF values near 1 (Riemer et al., 2010; Zhang et al., 2016).

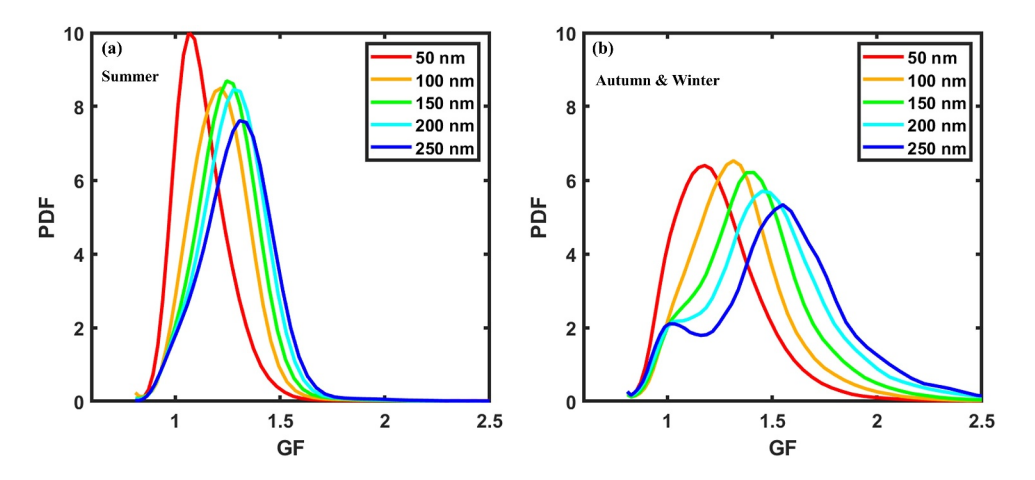
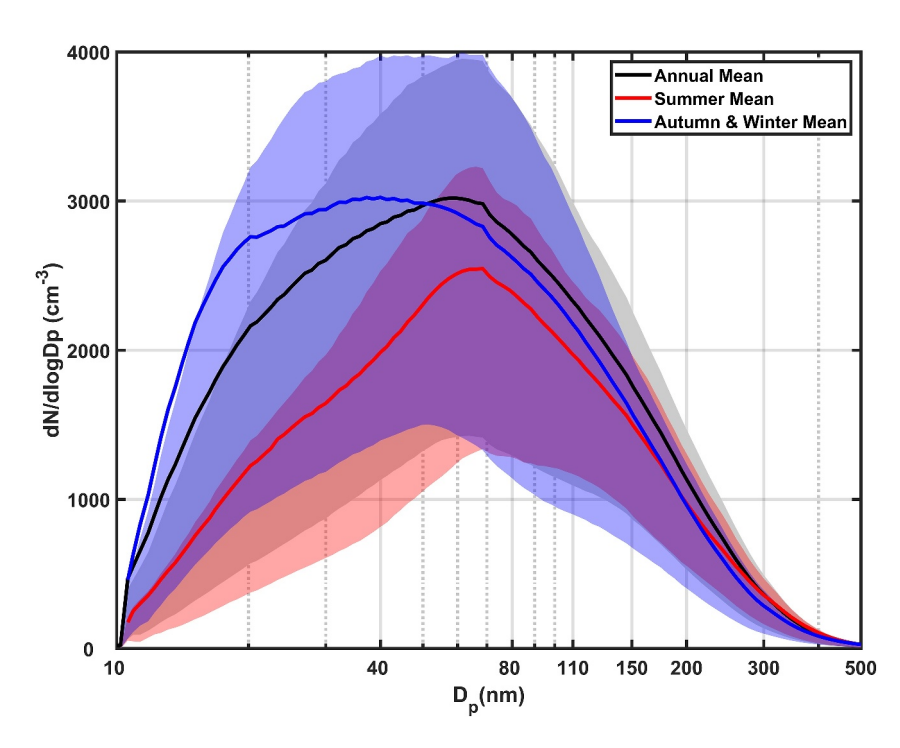


Figure 2. Average probability distributions of aerosol hygroscopic growth factor (GF-PDF) in (a) summer and (b) autumn and winter for five particle sizes (50, 100, 150, 200, and 250 nm).

HU ET AL. 6 of 18

21698996, 2025, 17, Downloaded from https://agupubs.onlinelibrary.wiley.com/doi/10.1029/2024JD041925 by Zhanqing Li - University Of Maryland , Wiley Online Library on [10/09/2025]. See



**Figure 3.** Average aerosol number concentration spectrum distributions, where black represents the annual average, red represents the summer average, and blue represents the autumn-winter average. The shaded areas represent the interquartile range (25th–75th percentile).

In Figure S5b in Supporting Information S1, the aerosol number concentration spectra obtained from the AOSNANOSMPS data set (Kuang et al., 2024) shows a characteristic pattern, with rapid growth from small to large particle sizes throughout the year. This is typically driven by nucleation processes involving sulfuric acid and ammonia, leading to the formation of 1 nm particles (Marinescu et al., 2019). J. Wang et al. (2006) found that high daytime aerosol number concentrations in the SGP are closely associated with gas precursors such as sulfur dioxide, which are critical for the formation of sulfate aerosols.

Seasonal variations in the aerosol number and mass concentrations are depicted in Figure S6 in Supporting Information S1. During summer, lower number concentrations and higher mass concentrations are observed, particularly in the 40–100 nm range. In contrast, during autumn and winter, high mass concentrations are noted in the mornings with low number concentrations, which significantly rise by afternoon. These seasonal differences highlight the potential impact of temperature on nucleation processes. Liu et al. (2021) suggest that the semi-volatile nature of aerosols causes higher temperatures to shift the equilibrium toward the gas phase, thereby reducing nitrate concentrations. This implies that in summer, higher temperatures increase volatility and reduce gas-to-particle conversion. Conversely, in autumn and winter, lower temperatures inhibit this volatilization process, potentially promoting nucleation and increasing the number of small particles. Moreover, the variation in the volatility of aerosol number spectra between summer and autumn-winter, as shown in Figure 3, indicates changes in source strength and nucleation processes across seasons. The stable transport sources and peak concentrations at larger diameters (about 70 nm) during summer starkly contrast with the 40 nm peak diameters and higher number concentrations observed in autumn and winter.

An analysis of the aerosol chemical compositions from the AOSACSM data set (Zawadowicz et al., 2021) reveals a pronounced organic matter content during summer, transitioning from sulfate-dominated inorganics to nitrates in autumn and winter, akin to observations by Liu et al. (2021) at the SGP site. Summer aerosol compositions were dominated by organic matter (74%) and sulfates (18%), whereas in autumn and winter, nitrates (21%), sulfates (14%), and organic matter (52%) were predominant (Figure 4). These seasonal variations are reflected in the hygroscopicity parameter  $\kappa$ , which was calculated using an aerosol chemical ion combination scheme and the ZSR model (see Equations S5 and S6 in Supporting Information S1). The mean value of  $\kappa$  is 0.618 in summer and increases to 0.636 in autumn and winter. Furthermore, high sulfate content was observed in the inorganic fraction

HU ET AL. 7 of 18

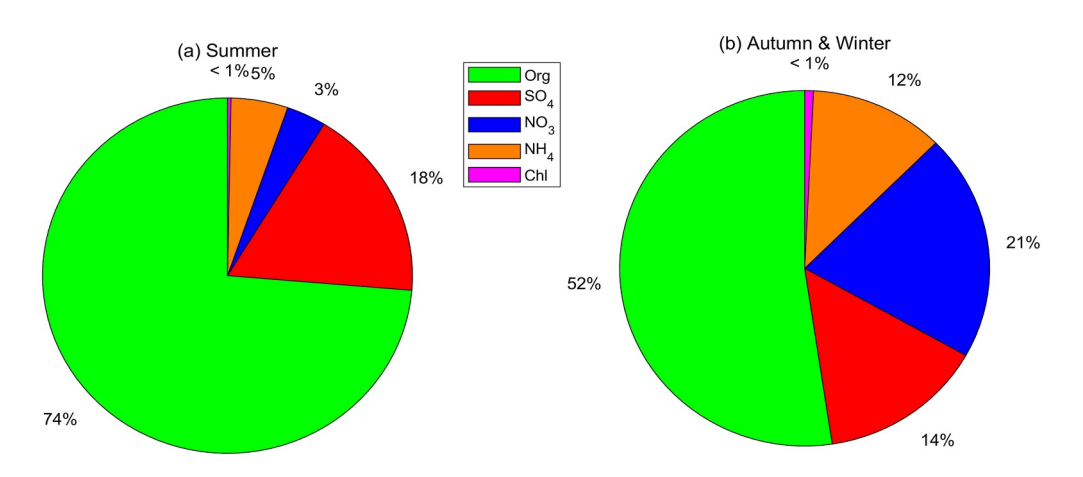


Figure 4. Proportions of PM1 chemical components observed by the ground-based aerosol chemical speciation monitor during (a) summer and (b) winter.

during both seasons, indicating significant influence from nearby coal-fired power plant sulfur emissions. The elevated organic matter content in summer can be attributed to intense biogenic emissions related to solar radiation and temperature, as well as sulfate nucleation-dominated photochemical processes (Parworth et al., 2015). The stronger acidic environment in summer aerosols inhibits nitrate formation, resulting in lower nitrate concentrations (Guo et al., 2016, 2017). In contrast, increased inorganic content during autumn and winter enhances aerosol hygroscopicity, which is linked to the rise in nitrates and other inorganic species.

#### 4.2. Optical Properties of Aerosols in the SCTZ

To explore variations in the optical properties of aerosols beneath clouds at different vertical distances from the cloud base, we compared the RH with  $\beta$  at 355 nm as a function of the vertical distance below the cloud base. Considering the significant variations in annual data, using the average to represent overall data characteristics can be skewed by extreme values. Therefore, this section uses the median of the distribution range as a common comparison (Tackett & Di Girolamo, 2009).

Figure 5 illustrates the variation in radiosonde-measured relative humidity (RH<sub>RS</sub>) and the backscatter coefficient  $\beta$  with distance from the cloud base. The box plot shows the median (central line), the upper quartile (top of the box), the lower quartile (bottom of the box), and the whiskers representing the 5th–95th percentile range. This representation highlights the spread and variability of the data across different distances from the cloud base. The left blue axis represents RH<sub>RS</sub>, while the right red axis indicates  $\beta$ . The *x*-axis is distance from the cloud base, with medians values denoted by dashed lines. Within the 0–50-m range from the cloud base, RH<sub>RS</sub> reaches a peak of approximately 92.67% and gradually decreases to 77.79% at distances beyond 450 m. Concurrently,  $\beta$  sharply increases within 250 m below the cloud base as the distance decreases, especially within the 0–50 m range rises to approximately 0.0083 km<sup>-1</sup> sr<sup>-1</sup>, which is about 3.5 times the value observed at the 350–400-m range (0.0024 km<sup>-1</sup> sr<sup>-1</sup>). The enhanced backscattering maybe caused by (a) the hygroscopic growth of aerosols, (b) the involvement of cloud fragments, and (c) changes in aerosol quantity and size. The similar behavior of  $\beta$  growth to the aerosol hygroscopic growth process, in the context of high environmental RH, suggests that hygroscopic growth of aerosols maybe a dominant factor near the cloud base. Y. Wang et al. (2023) also confirmed in their 2016 aircraft observations that aerosol size increases with altitude, with no significant difference in chemical composition.

However, as shown in Figure S8 in Supporting Information S1, the linear depolarization ratio (DR) of aerosols only shows a slight increase when the distance from the cloud base decreases from 50-100 to 0-50 m, with no significant overall changes. Specifically, DR rises modestly from 0.0217 in the 450-500-m range to 0.0234 at 150-200 m, and then slightly decreases to 0.0220 in the 50-100-m range, before increasing again to 0.0239 in the 0-50-m range close to the cloud base. This limited variation in DR, compared to the marked increase in the backscatter coefficient ( $\beta$ ), suggests that the overall shape of aerosols remains largely unchanged toward the cloud base. Since aerosols become more spherical upon hygroscopic growth, this indicates that hygroscopic growth may not be the sole or the dominant factor contributing to the increase in  $\beta$ . Aircraft observations support the presence

HU ET AL. 8 of 18

21698996, 2025, 17, Downloaded from https://agupubs.onlinelibrary.wiley.com/doi/10.1029/2024LD041925 by Zhanqing Li - University Of Maryland , Wiley Online Library on [10/09/2025]. See

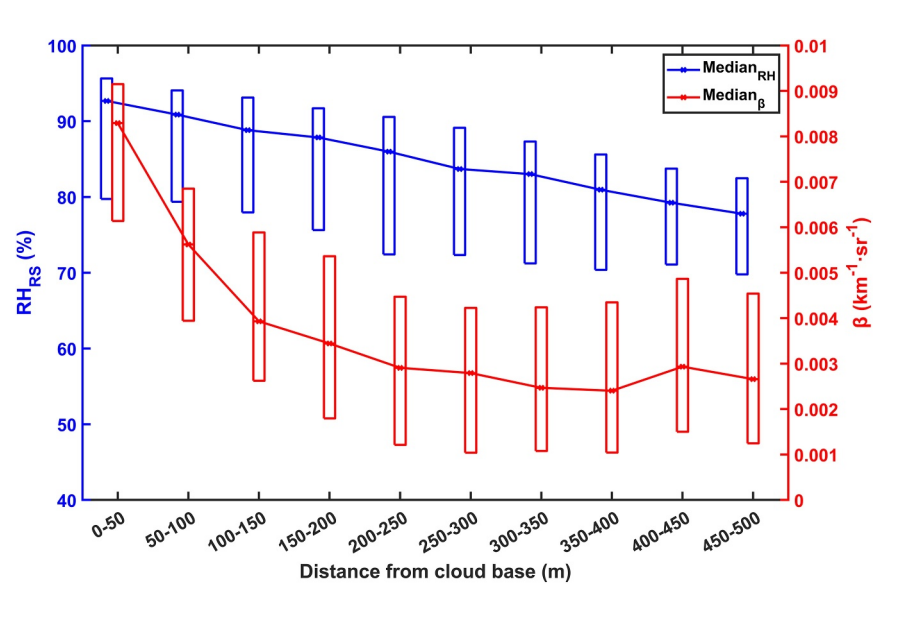


Figure 5. Box plot showing the variation of radiosonde-measured relative humidity (RH<sub>RS</sub>; left-hand axis; unit: %) and the aerosol backscatter coefficient ( $\beta$ ; right-hand axis; unit: km<sup>-1</sup> sr<sup>-1</sup>) with a distance from the cloud base. The box plot shows the median (central line), upper quartile (top of the box), lower quartile (bottom of the box), and whiskers representing the 5th–95th percentile range.

of hygroscopic growth at the cloud base (Huang & Lei, 2021); hence, the stability of DR and the fragmentation processes at the cloud base suggest that dispersed cloud fragments, resulting from entrainment and mixing, along with particle's hygroscopic growth, could also influence aerosol optical properties below the clouds could also influence aerosol optical properties, as well as any estimation of CCN from lidar backscattering measurements.

As illustrated in Figure 6, there are significant seasonal differences in the optical properties of aerosols in the SCTZ. In summer (Figure 6a), aerosol  $\beta$  values maintain around 0.002 km<sup>-1</sup> sr<sup>-1</sup> when the distance from the cloud base exceeds 250 m, and then rapidly increases to 0.0086 km<sup>-1</sup> sr<sup>-1</sup> as the distance decreases, which is a 5.4-fold increase, which exceeds the overall average increase of 3.5 times. In contrast, during autumn and winter (Figure 6b), the increase in aerosol  $\beta$  values is more modest, rising from 0.0024 to 0.0069 km<sup>-1</sup> sr<sup>-1</sup>, a 2.9-fold increase. The DR decreases with decreasing distance from the cloud base, especially in the range of 0–150 m, indicating that hygroscopic growth of aerosols may contribute more to the increase in  $\beta$  during autumn and winter.

A comparison between summer and autumn-winter data shows that the increase in  $\beta$  with decreasing cloud base distance is more pronounced in summer, whereas the reduction in DR during autumn-winter indicates a more significant influence of aerosol hygroscopic growth. As indicated by Figure S9 in Supporting Information S1, there is no significant difference in environmental RH, suggesting that the increase in  $\beta$  during autumn and winter is primarily due to stronger aerosol hygroscopic growth. Assuming that the contribution to the increase in  $\beta$  during autumn and winter is solely from aerosol hygroscopic growth, and if the hygroscopicity of summer aerosols was as strong as during autumn-winter, the contribution to  $\beta$  increase due to cloud fragments in summer compared to 300 m from the cloud base would be at least 2.5 times. Considering that autumn and winter do not solely experience hygroscopic growth and that the hygroscopicity of summer aerosols is weaker than that in autumn and winter, this underestimates the role of cloud fragments.

#### 4.3. Case Studies of Aerosol Hygroscopic Growth

To quantitatively compare the contributions of aerosol hygroscopic growth and cloud fragments to the increase in  $\beta$ , individual cases were selected where aerosol mixtures were uniform in terms of type, quantity, and size at specific altitude layers (Figure 7). Two cases were selected: one on 8 July 2021 (Case I) and the other on 29 July 2021 (Case II) at the closest time of the radiosonde launch time. According to Table 1, both cases within the study range meet the criteria for uniform vertical mixing of the atmosphere, as indicated by the vertical rate of change of w and  $\theta$  per kilometer.

HU ET AL. 9 of 18

21698996, 2025, 17, Downloaded from https://agupubs.onlinelibrary.wiley.com/doi/10.1029/2024JD041925 by Zhanqing Li - University Of Maryland , Wiley Online Library on [10/09/2025]. See the Terms

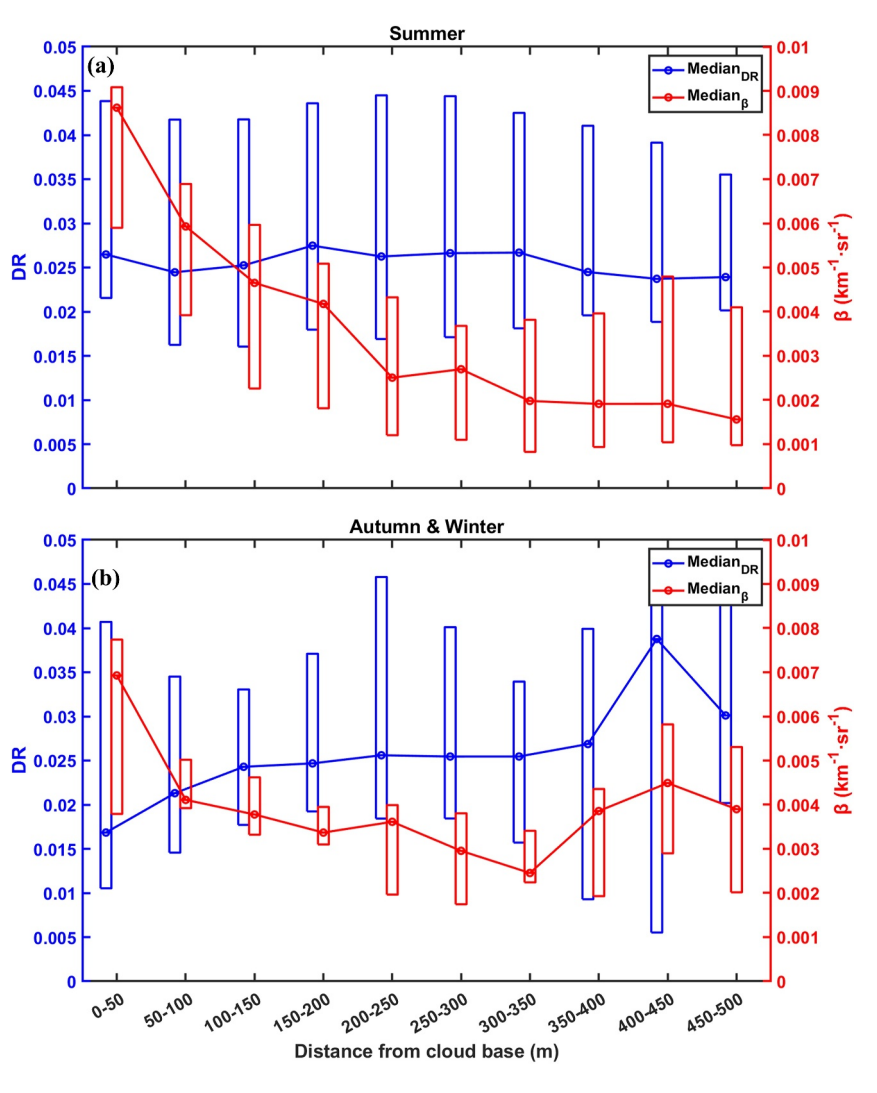


**Figure 6.** (a) Summer and (b) autumn-winter seasonal variations in the depolarization ratio (DR; left-hand axis) and aerosol backscatter coefficient ( $\beta$ ; right-hand axis; unit: km<sup>-1</sup> sr<sup>-1</sup>) with respect to the distance below cloud base, depicted in box plots

In the altitude range beneath the clouds, as the altitude increased and the distance from the cloud base decreased, the radiosonde-measured RH (Figures 7c and 7j for Cases I and II, respectively) and  $\beta_{355}$  (Figures 7e and 7l for Cases I and II, respectively) continually increased, and DR decreased (Figures 7g and 7n for Cases I and II, respectively). This indicates that the aerosols underwent hygroscopic growth as RH increased, gradually becoming more spherical in shape (Bedoya-Velásquez et al., 2018; Chen et al., 2019; Granados-Muñoz et al., 2015; Lv et al., 2017). Furthermore, Table 1 shows that the lidar ratio fluctuated between 70 and 90 in Case I, while in Case II, it was around 75. These lidar ratio values suggest that the aerosol type was likely predominantly continental clean in these instances, as typical lidar ratios for continental aerosols fall within this range (Ferrare et al., 2001).

Based on the  $\beta_{355}$  and RH<sub>RS</sub> profiles, the hygroscopic GF,  $f_{\beta}(RH)$ , can be computed using Equation 1. For this analysis, the reference relative humidity (RH<sub>ref</sub>) is set at 75% for Case I and 65% for Case II. Subsequent parameterization fits to the aerosol hygroscopic growth enhancements were conducted using Equations 2 and 3, with the results depicted in Figure 8. Table 2 presents the fit outcomes for the two parameterization schemes, where the coefficient of determination ( $R^2$ ) serves as an indicator of fitness; a higher  $R^2$  value indicates a stronger correlation. Notably, Kasten's biparametric scheme demonstrated superior correlation. Additionally, the magnitude of the hygroscopicity parameters  $\gamma$  and b directly reflects the degree of aerosol hygroscopicity. Case II

HU ET AL. 10 of 18

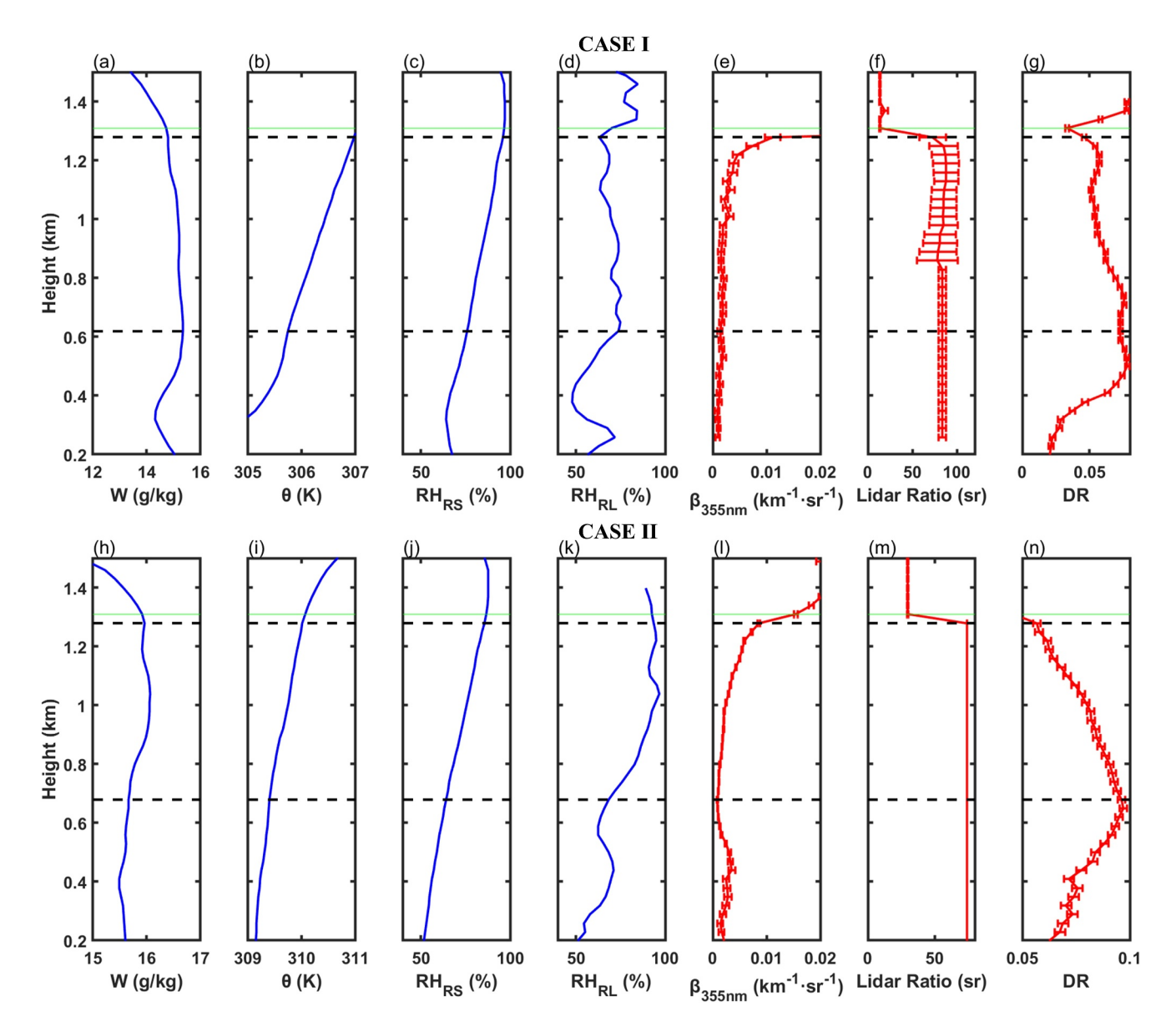


Figure 7. Case I (top row) and Case II (bottom row) profiles of (a and h) water vapor mixing ratio (w), (b and i) potential temperature ( $\theta$ ), (c and j) radiosonde relative humidity (RH<sub>RS</sub>), (d and k) Raman lidar relative humidity (RH<sub>RL</sub>), (e and l) backscatter coefficient at 355 nm ( $\beta_{355nm}$ ), (f and m) lidar ratio at 355 nm, and (g and n) depolarization ratio at 355 nm. Black dashed lines represent the altitude range for the case studies, and green solid lines indicate the lowest cloud base height. Horizontal error bars represent the uncertainty of the parameters.

aerosols exhibited stronger hygroscopic properties than those in Case I, suggesting more rapid hygroscopic growth in environments with higher RH.

To further elucidate differences in aerosol types between the two cases, a 48-hr backward trajectory analysis using the HYSPLIT model (NOAA Air Resources Laboratory, 2024), as shown in Figure S10 in Supporting Information S1, revealed that the aerosols in Case I predominantly originated from natural sources on the northwestern grasslands, with surface aerosols primarily composed of nitrates and sulfates. In contrast, Case II aerosols are mainly from anthropogenic sources in the southern power plants and urban areas, characterized predominantly by sulfate aerosols. The consistency in the chemical composition of boundary layer aerosols (Y. Wang et al., 2023) suggests that this may lead to the stronger hygroscopicity observed in Case II aerosols compared to Case I.

Upon recalibrating RH<sub>ref</sub> to 40% as per Equation 4, the optical enhancement factors at RH of 80%, denoted as  $f_{\text{ref}=40\%}$  (80%), are compared between the two cases. The results are shown in Figure S11 in Supporting

HU ET AL. 11 of 18

**Table 1**Case I and II Gradient Values Within the Study Altitude Range for Water Vapor Mixing Ratio (w), Potential Temperature ( $\theta$ ), Radiosonde Relative Humidity (RH<sub>RS</sub>), Raman Lidar Relative Humidity (RH<sub>RL</sub>), Aerosol Backscatter Coefficient ( $\beta_{355}$ ), and Depolarization Ratio (DR) at 355 nm

		Case I			Case II			
	Range		Gradient (km <sup>-1</sup> )	Rai	nge	Gradient (km <sup>-1</sup> )		
Height (km)	0.6187	1.2787	-	0.6787	1.2787	-		
w (g/kg)	15.353	14.804	-0.832	15.668	15.958	0.483		
$\theta$ (K)	305.747	307.000	1.898	309.400	310.014	1.023		
$RH_{RS}$ (%)	75.830	95.952	-	64.127	85.527	-		
$\mathrm{RH}_{\mathrm{RL}}$ (%)	73.868	75.180	-	68.114	93.295	-		
$\beta_{355}  (\mathrm{km^{-1} \ sr^{-1}})$	0.0012	0.0111	_	0.0008	0.0086	-		
DR	0.0730	0.0460	-0.041	0.0961	0.0567	-0.066		

Information S1, showing that the enhancement factor for Case I is approximately 4, whereas for Case II, it is about 17, demonstrating significantly stronger hygroscopic properties of aerosols in Case II. This aligns with the anthropogenic characteristics and high hygroscopicity of the aerosols in Case II. However, both the hygroscopic enhancement factors and hygroscopicity parameters far exceed the values typically associated with traditional sea salt aerosols (Haarig et al., 2017), which are generally known for their high hygroscopic enhancement. This suggests that the elevated backscatter coefficients observed below the cloud may not solely be attributable to aerosol hygroscopic growth but could involve other types of aerosol or additional factors.

Considering the observed increase in DR near cloud bases, a portion of the enhanced backscatter coefficient maybe attributed to presence of irregular cloud fragments, including small cloud droplets, virga, and processed aerosols generated by cloud fragmentation effects. Notably, in Case II, around RH = 75%, a transition resembling a deliquescence point occurs, indicating aerosol activation. Beyond RH = 80%, the rate of increase in the hygroscopic enhancement factor slows, likely due to the transformation of aerosols into CCN that consume inorganic components at the cloud base (Sicard et al., 2022). This activation of aerosols into clouds could also contribute to the increase in backscatter coefficients.

The situation of cloud fragments enhancing  $\beta$  was further examined by comparing aerosol optical property profiles before and after the Case II cloud instance. Assuming that the vertical mixing state of aerosols does not change over a short period, as shown in Figure 9, the optical properties of aerosols under clouds were observed 3 hr before and after the cloud point in time (17:35 UTC on 29 July 2021). Figure 9a shows that a new cloud appeared 2 hr after the Case II cloud, potentially introducing cloud interference. Within the subcloud altitude range of 0–1.5 km, no new clouds were observed 1 hr before and after the Case II cloud event, ensuring minimal interference. Additionally, as shown in Figure 9c and referenced in Figure 5, the rapid hygroscopic growth phase

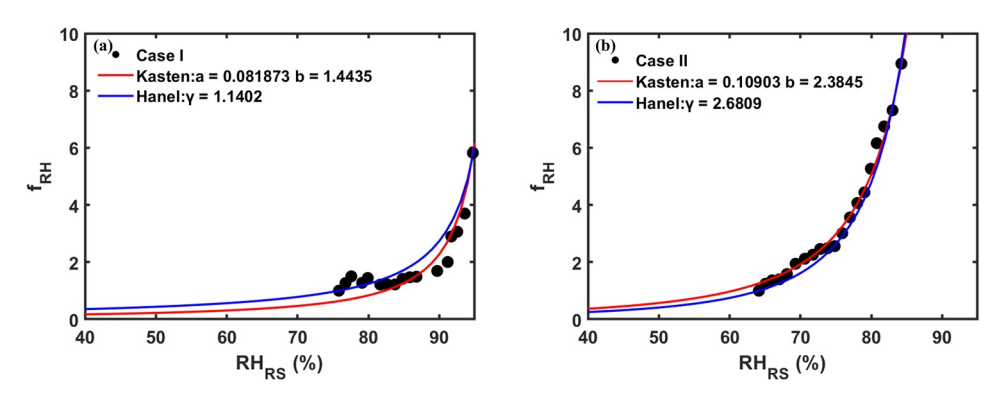


**Figure 8.** For (a) Case I (aerosol layer: 0.6187–1.2787 km) and (b) Case II (aerosol layer: 0.6787–1.2787 km), variations in the hygroscopic enhancement factor of the 355 nm backscatter coefficient relative to radiosonde humidity are depicted. The red and blue lines correspond to fits using the Kasten and Hänel models, respectively.

HU ET AL. 12 of 18

	Case I			Case II		
Kasten	a	b	$R^2$	a	b	$R^2$
	0.068	1.504	0.951	0.109	2.384	0.993
Hänel	γ		$R^2$	γ		$R^2$
1.139		139	0.911	2.680		0.980

occurs within approximately 150 m of the cloud base; Figures 9c and 9d also indicate that stable DR and  $\beta$  values in the 1.5–1.65 km range within the hour following 17:35 UTC. Therefore, we selected aerosol optical properties within 1 hr before and after the Case II cloud were selected for statistical analysis and compared with conditions under the steady cloud.

Assuming that the RH and uniform mixing state remained unchanged within the selected time frame, it was necessary to compare w,  $\theta$ , and RH below (cloudy) and before-after the cloud (noncloudy). The results are shown in Figure 10a, where the horizontal axis represents RH<sub>RS</sub> at the same altitude, the left blue axis represents the average water vapor mixing ratio derived

using the RL, red denotes the average potential temperature, large circles represent below-cloud data, small circles represent above-cloud data, and vertical bars are the standard deviations. The trends in the average values of both w and  $\theta$  are consistent regardless of cloud presence, with deviations not exceeding 2, suggesting that the overall distributions of w and  $\theta$  are essentially consistent with the homogeneous layer distributions of the original radiosonde. Therefore, it can be confirmed that the assumption of uniform mixing in the SCTZ within 1 hr before and after is valid.

According to Figure 10b, before the corresponding radiosonde  $RH_{RS} = 75\%$ , the RH detected by Raman shows little change whether below or outside the cloud, demonstrating good consistency. However, when RH becomes higher, the below-noncloud RH represented by red is slightly lower than that below the cloud. Notably in Figure 10a, when RH is high (close to the cloud base), w below the cloud is higher than that outside. This difference can be attributed primarily to the temperature decrease with altitude, which increases RH near the cloud base without requiring downward diffusion of water vapor. This confirms that the aerosol and environmental conditions below and outside the cloud are consistent.

Observations from Figures 10c and 10d reveal that aerosol optical properties vary with RH, maintaining a consistent  $\beta$  of 0.001 km<sup>-1</sup> sr<sup>-1</sup> at low RH (<65%) for both cloud-affected and noncloud-affected profiles, indicating stable aerosol characteristics within the selected time frame. Upon humidification to RH = 85%, the average  $\beta$  under cloudy conditions increases to 0.0035 km<sup>-1</sup> sr<sup>-1</sup>, approximately 50% higher than the 0.0023 km<sup>-1</sup> sr<sup>-1</sup> observed in noncloud conditions. Given the stability of aerosol chemical composition and number concentration, this enhancement in  $\beta$  beneath clouds is likely attributable to cloud fragments, with the degree of enhancement increasing with proximity to the cloud base. Furthermore, the trend of decreasing DR in Figure 10d corroborates this observation; while DR decreases with rising RH across all profiles, the rate of decrease is slower under cloudy conditions. The finding suggests that irregular particles, likely originating from fragmented cloud droplets at the cloud base, may contribute to the observed changes in aerosol properties. These

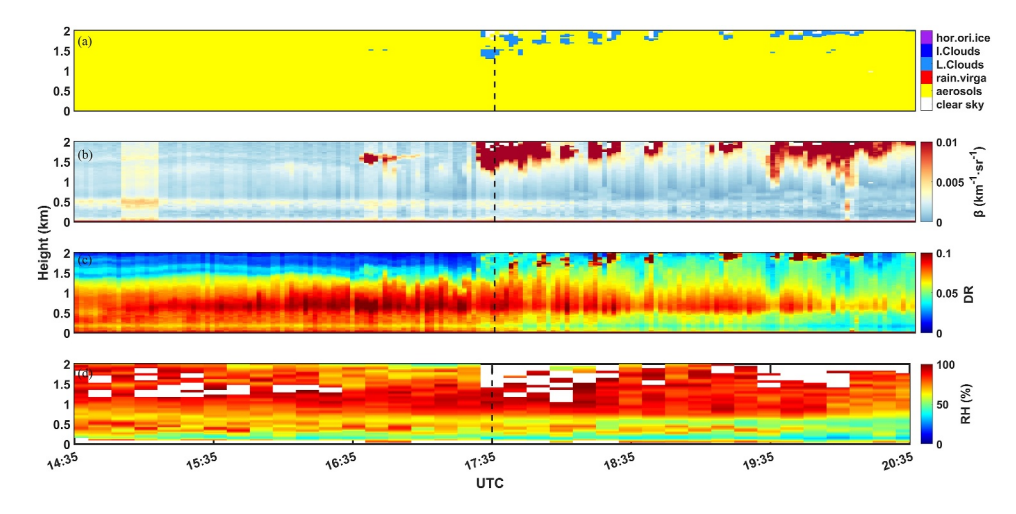


Figure 9. Time series plot for 3 hr before and after the Case II moment, featuring (a) cloud feature identification (light blue for water clouds and yellow for aerosols), (b) aerosol backscatter coefficient  $(\beta)$ , (c) depolarization ratio, and (d) Raman Lidar relative humidity. The dashed lines indicate moments when measurements were taken by a radiosonde.

HU ET AL. 13 of 18

21698996, 2025, 17, Downloaded from https://agupubs.onlinelibrary.wiley.com/doi/10.1029/2024JD041925 by Zhanqing Li - University Of Maryland , Wiley Online Library on [10/09/2025]. See the Term

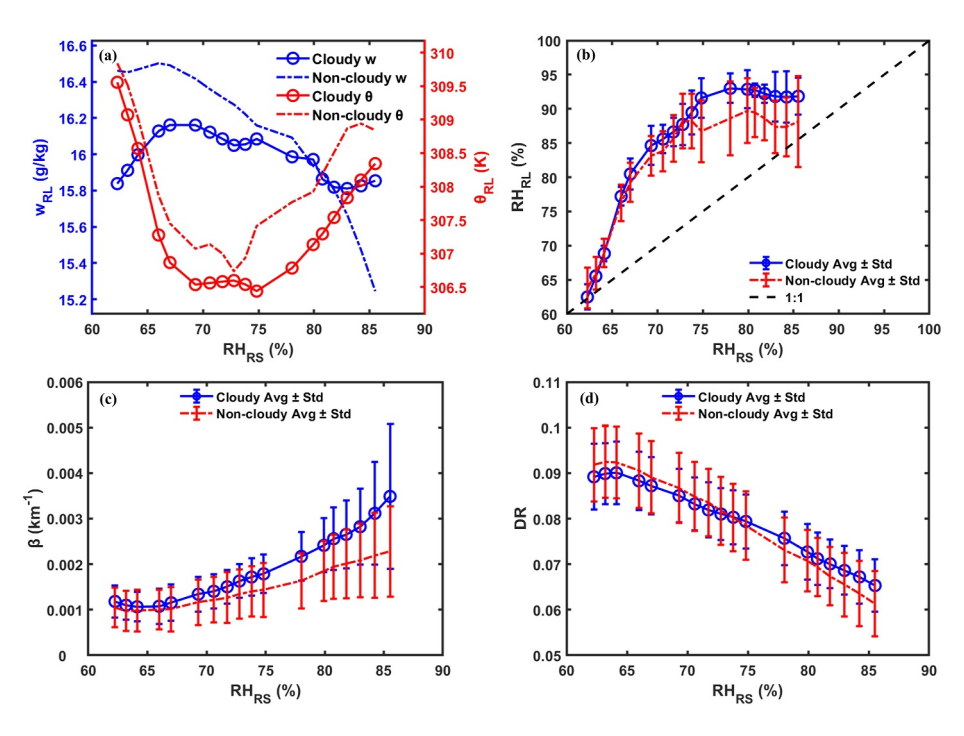


Figure 10. Variations of physical parameters within 1 hr before and after the CASE II moment with respect to radiosonde relative humidity (RH<sub>RS</sub>): (a) blue represents the water vapor mixing ratio (w) and red represents potential temperature ( $\theta$ ), (b) relative humidity (RH<sub>RL</sub>) detected using a Raman lidar, (c) aerosol backscatter coefficient ( $\beta$ ), and (d) aerosol depolarization ratio. Here, "o" denotes below-cloud and "." denotes nonbelow-cloud conditions.

fragments, resulting from cloud droplet breakup or entrainment processes, can affect particle shape and increase scattering or depolarization ratios, setting them apart from typical spherical aerosols.

Based on the results of aerosol optical hygroscopicity parameter fits presented in Figure 11 and Table 3, the hygroscopic GF at reference RH from 65% to 85% ( $f_{\rm ref=65\%}(85\%)$ ) is 2.8 under cloudy conditions and 2.2 under noncloudy conditions. Assuming that the enhancement of  $\beta$  near the cloud base under noncloudy is solely driven by aerosol hygroscopic growth, the contribution of cloud fragments to  $\beta$  enhancement in cloud-influenced regions is approximately 33.3%, while aerosol hygroscopic growth accounts for 66.7%. If we do not distinguish between contributions from cloud fragments and aerosol hygroscopic growth, the optical hygroscopicity parameters for

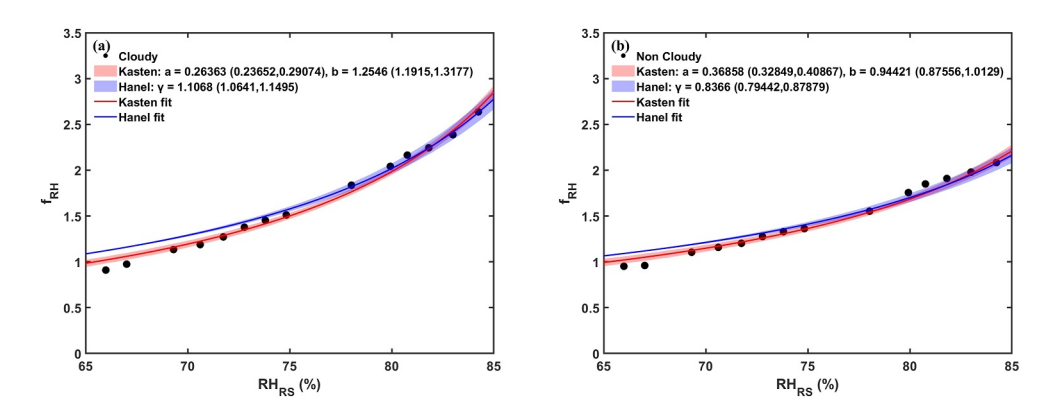


Figure 11. Variation of the hygroscopic enhancement factor for the aerosol backscatter coefficient ( $\beta$ ) at a wavelength of 355 nm as a function of radiosonde relative humidity (RH<sub>RS</sub>) for (a) cloudy and (b) noncloudy conditions. The red and blue lines represent the parameterized fitting curves using the Kasten and Hänel models, respectively, with shaded areas indicating the 95% confidence intervals.

HU ET AL. 14 of 18

**Table 3**Parameters and R<sup>2</sup> Values for the Kasten and Hänel Model Fittings for Cloudy and Clear-Sky Conditions During the Period of 1 hr Before and After the Case II Cloud Point in Time (17:35 UTC on 29 July 2021)

		Cloudy			Noncloudy	
Kasten	a	b	$R^2$	a	b	$R^2$
	0.284 (±0.027)	1.255 (±0.063)	0.992	0.369 (±0.040)	0.944 (±0.069)	0.982
Hänel	γ		$R^2$	γ		$R^2$
	1.107 (±0.043)		0.976	$0.837 (\pm 0.042)$		0.965

particles under clouds are greater than those under noncloudy conditions, indicating stronger hygroscopicity of aerosols under cloudy conditions.

# 5. Summary and Conclusions

This study utilized 1 year of ground and below-cloud aerosol observation data (28 April 2021–23 April 2022) from the SGP supersite, part of the Department of Energy's Atmospheric Radiation Measurement (ARM) program, to examine in detail the effects of seasonal changes on aerosol hygroscopicity and optical properties. The research particularly focused on the impact of cloud fragments in the SCTZ on the aerosol backscatter coefficient  $(\beta)$ , leading to the following main conclusions.

Meteorological conditions showed clear seasonal patterns at the site, characterized by a hot and humid summer and cold yet still humid autumn and winter. The decrease in fine particulate matter during summer may result from high temperatures suppressing gas-to-particle conversion (Liu et al., 2021). The hygroscopic characteristics of aerosols, such as the hygroscopic GF, also showed clear seasonal differences. In summer, aerosols were mostly internally mixed organics with weaker hygroscopicity, primarily influenced by anthropogenic emissions from the southeast. By contrast, aerosols in autumn and winter exhibited a higher degree of aging and stronger hygroscopicity, influenced by both biogenic emissions from the northwest and anthropogenic sources from the southeast. Due to a higher proportion of inorganic matter, autumn and winter aerosols exhibited stronger hygroscopicity than those in summer.

In-depth analysis of the hygroscopicity and optical properties of aerosols in the SCTZ, based on RL and radiosonde measurements, revealed significant increases in the aerosol backscattering coefficient ( $\beta$ ) and RH as the distance from the cloud base decreased. This phenomenon is primarily driven by aerosol hygroscopic growth and contributions from cloud fragments. Comparisons between summer and autumn/winter showed that the near-cloud enhancement effect was especially pronounced in summer, likely due to more frequent cloud fragmentation processes at the bases of convective clouds. Case studies comparing aerosol optical properties under cloud-covered and cloud-free conditions revealed that about 33.3% of the enhancement in the aerosol backscattering coefficient could be attributed to cloud fragments, while the remaining 66.7% was contributed by aerosol hygroscopic growth. Furthermore, aerosol activation into clouds near the cloud base was also observed, which may also contribute to the enhanced backscattering coefficients.

In summary, this study delineates the impact of seasonal variations on aerosol properties within the SCTZ, with particular attention to the role of cloud fragments in modifying  $\beta$ . These observations reveal a complex interaction between aerosol hygroscopicity and cloud fragments. Importantly, when the effects of cloud fragments are not differentiated, subcloud aerosol hygroscopicity appears more pronounced in summer and less so in autumn and winter, presenting an inverse pattern compared to ground-level observations. This insight is crucial for understanding the influence of seasonal and vertical variations on aerosol properties during cloud transitions and highlights the significant role of cloud fragments in influencing aerosol measurements in the SCTZ.

While this study primarily focused on specific case studies, additional statistical analyses and calculations of radiative effects are warranted to further explore the aerosol climate effects associated with significant variations in aerosol optical properties observed in the TZ. Future work should seek more uniformly mixed subcloud cases to validate and expand upon these conclusions, enhancing the predictive capabilities of atmospheric radiation models and our overall comprehension of aerosol-cloud interactions.

HU ET AL. 15 of 18

### **Data Availability Statement**

All data sets used in this study were obtained from the Atmospheric Radiation Measurement (ARM) User Facility, a U.S. Department of Energy (DOE) Office of Science user facility, and are publicly available through the ARM Data Center. The following ARM data sets were used:

- ACSM composition-corrected aerosol mass concentrations (ACSMCDCE) at SGP E13 [Data set]. https://doi. org/10.5439/1763029
- Surface meteorological measurements (MET) at SGP E13 [Data set]. https://doi.org/10.5439/1786358
- Raman lidar feature mask profiles (RLPROFFEXAUX1THOR) at SGP C1 [Data set]. https://doi.org/10.5439/ 1373940
- Scanning Mobility Particle Sizer data (AOSSMPS) at SGP E13 [Data set]. https://doi.org/10.5439/1476898
- Aerosol hygroscopicity data from the Humidified Tandem Differential Mobility Analyzer (AOSHTDMA) at SGP E13 [Data set]. https://doi.org/10.5439/1776643

Backward trajectories were computed using the HYSPLIT model developed by the NOAA Air Resources Laboratory, which is freely accessible at https://www.ready.noaa.gov/ [Software]

All data sets and software are cited in the reference list with appropriate [Data set] and [Software] tags in accordance with AGU data availability policy.

#### Acknowledgments References

Data from the U.S. Department of Energy as part of the Atmospheric Radiation Measurement (ARM) User Facility at the South Great Plain were used.

Balmes, K. A., Fu, Q., & Thorsen, T. J. (2021). The diurnal variation of the aerosol optical depth at the ARM SGP site. *Earth and Space Science*, 8(10), e2021EA001852. https://doi.org/10.1029/2021ea001852

Bar-Or, R. Z., Altaratz, O., & Koren, I. (2011). Global analysis of cloud field coverage and radiative properties, using morphological methods and MODIS observations. *Atmospheric Chemistry and Physics*, 11(1), 191–200. https://doi.org/10.5194/acp-11-191-2011

Bar-Or, R. Z., Koren, I., Altaratz, O., & Fredj, E. (2012). Radiative properties of humidified aerosols in cloudy environment. Atmospheric Research, 118, 280–294. https://doi.org/10.1016/j.atmosres.2012.07.014

Bedoya-Velásquez, A. E., Navas-Guzmán, F., Granados-Muñoz, M. J., Titos, G., Román, R., Casquero-Vera, J. A., et al. (2018). Hygroscopic growth study in the framework of EARLINET during the SLOPE I campaign: Synergy of remote sensing and in situ instrumentation. *Atmospheric Chemistry and Physics*, 18(10), 7001–7017. https://doi.org/10.5194/acp-18-7001-2018

Calbó, J., Long, C. N., González, J., Augustine, J., & McComiskey, A. (2017). The thin border between cloud and aerosol: Sensitivity of several ground based observation techniques. *Atmospheric Research*, 196, 248–260. https://doi.org/10.1016/j.atmosres.2017.06.010

Chen, J., Li, Z., Lv, M., Wang, Y., Wang, W., Zhang, Y., et al. (2019). Aerosol hygroscopic growth, contributing factors, and impact on haze events in a severely polluted region in northern China. *Atmospheric Chemistry and Physics*, 19(2), 1327–1342. https://doi.org/10.5194/acp-19-1327-2019

Cromwell, E., Newsom, R., Zhang, D., & Chand, D. (2023). Raman lidar vertical profiles feature detection and extinction (RLPROFFEX-AUX1THOR), southern great plains (SGP), central facility, Lamont, OK (C1) [Dataset]. Atmospheric Radiation Measurement (ARM) User Facility. https://doi.org/10.5439/1373940

Eck, T. F., Holben, B. N., Reid, J. S., Arola, A., Ferrare, R. A., Hostetler, C. A., et al. (2014). Observations of rapid aerosol optical depth enhancements in the vicinity of polluted cumulus clouds. *Atmospheric Chemistry and Physics*, 14(21), 11633–11656. https://doi.org/10.5194/acp-14-11633-2014

Eytan, E., Koren, I., Altaratz, O., Kostinski, A. B., & Ronen, A. (2020). Longwave radiative effect of the cloud twilight zone. *Nature Geoscience*, 13(10), 669–673. https://doi.org/10.1038/s41561-020-0636-8

Fernández, A. J., Apituley, A., Veselovskii, I., Suvorina, A., Henzing, J., Pujadas, M., & Artíñano, B. (2015). Study of aerosol hygroscopic events over the Cabauw experimental site for atmospheric research (CESAR) using the multi-wavelength Raman lidar Caeli. *Atmospheric Environment*, 120, 484–498. https://doi.org/10.1016/j.atmosenv.2015.08.079

Ferrare, R., Clayton, M., Turner, D., Newsom, R., & Scarino, A. J. (2013). Raman lidar retrievals of mixed layer heights over the TWP Darwin and SGP sites. In *Proceedings of the ASR science team meeting, Potomac, MD*.

Ferrare, R., Turner, D., Clayton, M., Schmid, B., Redemann, J., Covert, D., et al. (2006). Evaluation of daytime measurements of aerosols and water vapor made by an operational Raman lidar over the southern great plains. *Journal of Geophysical Research*, 111(D5), D05S08. https://doi.org/10.1029/2005JD005836

Ferrare, R. A., Turner, D. D., Brasseur, L. H., Feltz, W. F., Dubovik, O., & Tooman, T. P. (2001). Raman lidar measurements of the aerosol extinction-to-backscatter ratio over the southern great plains. *Journal of Geophysical Research*, 106(D17), 20333–20347. https://doi.org/10.1029/2000ID000144

Granados-Muñoz, M. J., Navas-Guzmán, F., Bravo-Aranda, J. A., Guerrero-Rascado, J. L., Lyamani, H., Valenzuela, A., et al. (2015). Hygroscopic growth of atmospheric aerosol particles based on active remote sensing and radiosounding measurements: Selected cases in southeastern Spain. Atmospheric Measurement Techniques, 8(2), 705–718. https://doi.org/10.5194/amt-8-705-2015

Gristey, J. J., Feingold, G., Glenn, I. B., Schmidt, K. S., & Chen, H. (2020). On the relationship between shallow cumulus cloud field properties and surface solar irradiance. *Geophysical Research Letters*, 47(22), e2020GL090152. https://doi.org/10.1029/2020gl090152

Guo, H., Liu, J., Froyd, K. D., Roberts, J. M., Veres, P. R., Hayes, P. L., et al. (2017). Fine particle pH and gas-particle phase partitioning of inorganic species in Pasadena, California, during the 2010 CalNex campaign. Atmospheric Chemistry and Physics, 17(9), 5703–5719. https://doi.org/10.5194/acp-17-5703-2017

Guo, H., Sullivan, A. P., Campuzano Jost, P., Schroder, J. C., Lopez Hilfiker, F. D., Dibb, J. E., et al. (2016). Fine particle pH and the partitioning of nitric acid during winter in the northeastern United States. *Journal of Geophysical Research: Atmospheres*, 121(17), 10310–10376. https://doi.org/10.1002/2016JD025311

HU ET AL. 16 of 18

- Gysel, M., Crosier, J., Topping, D. O., Whitehead, J. D., Bower, K. N., Cubison, M. J., et al. (2007). Closure study between chemical composition and hygroscopic growth of aerosol particles during TORCH2. Atmospheric Chemistry and Physics, 7(24), 6131–6144. https://doi.org/10.5194/acp-7-6131-2007
- Haarig, M., Ansmann, A., Gasteiger, J., Kandler, K., Althausen, D., Baars, H., et al. (2017). Dry versus wet marine particle optical properties: RH dependence of depolarization ratio, backscatter, and extinction from multiwavelength lidar measurements during SALTRACE. Atmospheric Chemistry and Physics, 17(23), 14199–14217. https://doi.org/10.5194/acp-17-14199-2017
- Hänel, G. (1976). The properties of atmospheric aerosol particles as functions of the relative humidity at thermodynamic equilibrium with the surrounding moist air. In *Advances in geophysics* (pp. 73–188). Elsevier. https://doi.org/10.1016/S0065-2687(08)60142-9
- Hegg, D. A., Covert, D. S., Rood, M. J., & Hobbs, P. V. (1996). Measurements of aerosol optical properties in marine air. *Journal of Geophysical Research*, 101(D8), 12893–12903. https://doi.org/10.1029/96JD00751
- Huang, M., & Lei, H. (2021). Cloud particle shattering and its impact on cloud microphysical parameters' measurement in stratiform clouds with embedded convection. *Chinese Journal of Atmospheric Sciences*, 45, 369–378. https://doi.org/10.3878/j.issn.1006-9895.2006.19255
- Intergovernmental Panel on Climate Change (IPCC). (2013). In T. F. Stocker, D. Qin, G.-K. Plattner, M. Tignor, S. K. Allen & J. Boschung (Eds.), Climate change 2013: The physical science basis, the contribution of working group I to the fifth assessment report of the intergovernmental panel on climate change. Cambridge University Press.
- Intergovernmental Panel on Climate Change (IPCC). (2021). In V. Masson-Delmotte, P. Zhai, A. Pirani, S. L. Connors, C. Péan & S. Berger (Eds.), Climate change 2021: The physical science basis, the contribution of working group I to the sixth assessment report of the intergovernmental panel on climate change. Cambridge University Press.
- Jacobson, M. C., Hansson, H. C., Noone, K. J., & Charlson, R. J. (2000). Organic atmospheric aerosols: Review and state of the science. Reviews of Geophysics, 38(2), 267–294. https://doi.org/10.1029/1998RG000045
- Jahani, B., Calbó, J., & González, J. A. (2019). Transition zone radiative effects in shortwave radiation parameterizations: Case of weather research and forecasting model. *Journal of Geophysical Research: Atmospheres*, 124(23), 13091–13104. https://doi.org/10.1029/ 2019ID031064
- Jahani, B., Calbó, J., & González, J. A. (2020). Quantifying transition zone radiative effects in longwave radiation parameterizations. Geophysical Research Letters, 47(22), e2020GL090408. https://doi.org/10.1029/2020GL090408
- Jeong, M., & Li, Z. (2010). Separating real and apparent effects of cloud, humidity, and dynamics on aerosol optical thickness near cloud edges. Journal of Geophysical Research, 115(D7), D00K32. https://doi.org/10.1029/2009JD013547
- Kahn, R. A., Andrews, E., Brock, C. A., Chin, M., Feingold, G., Gettelman, A., et al. (2023). Reducing aerosol forcing uncertainty by combining models with satellite and within-the-atmosphere observations: A three-way street. *Reviews of Geophysics*, 61(2), e2022RG000796. https://doi.org/10.1029/2022RG000796
- Kaufman, Y. J., Remer, L. A., Tanre, D., Li, R., Kleidman, R., Mattoo, S., et al. (2005). A critical examination of the residual cloud contamination and diurnal sampling effects on MODIS estimates of aerosol over ocean. *IEEE Transactions on Geoscience and Remote Sensing*, 43(12), 2886–2897. https://doi.org/10.1109/TGRS.2005.858430
- Koren, I., Remer, L. A., Kaufman, Y. J., Rudich, Y., & Martins, J. V. (2007). On the twilight zone between clouds and aerosols. Geophysical Research Letters, 34(8), L8805. https://doi.org/10.1029/2007GL029253
- Kuang, C., Singh, A., Howie, J., Salwen, C., & Hayes, C. (2024). Scanning mobility particle sizer (AOSSMPS), southern great plains (SGP), Lamont, OK (extended and Co-located with C1) (E13) [Dataset]. Atmospheric Radiation Measurement (ARM) User Facility. https://doi.org/10. 5439/1476898
- Kyrouac, J., Shi, Y., & Tuftedal, M. (2023). Surface meteorological instrumentation (MET), southern great plains (SGP), Lamont, OK (extended and Co-located with C1) (E13) [Dataset]. Atmospheric Radiation Measurement (ARM) User Facility. https://doi.org/10.5439/1786358
- Li, Z., Li, C., Chen, H., Tsay, S. C., Holben, B., Huang, J., et al. (2011). East Asian studies of tropospheric aerosols and their impact on regional climate (EAST-AIRC): An overview. *Journal of Geophysical Research*, 116, D00K34. https://doi.org/10.1029/2010JD015257
- Li, Z., Rosenfeld, D., & Fan, J. (2017). Aerosols and their impact on radiation, clouds, precipitation, and severe weather events. Oxford Research Encyclopedia of Environmental Science.
- Liu, J., Alexander, L., Fast, J. D., Lindenmaier, R., & Shilling, J. E. (2021). Aerosol characteristics at the southern great plains site during the HI-SCALE campaign. Atmospheric Chemistry and Physics, 21(6), 5101–5116. https://doi.org/10.5194/acp-21-5101-2021
- Liu, J., & Li, Z. (2018). First surface-based estimation of the aerosol indirect effect over a site in southeastern China. Advances in Atmospheric Sciences, 35(2), 169–181. https://doi.org/10.1007/s00376-017-7106-2
- Lv, M., Liu, D., Li, Z., Mao, J., Sun, Y., Wang, Z., et al. (2017). Hygroscopic growth of atmospheric aerosol particles based on lidar, radiosonde, and in situ measurements: Case studies from the Xinzhou field campaign. *Journal of Quantitative Spectroscopy and Radiative Transfer*, 188, 60–70. https://doi.org/10.1016/j.jqsrt.2015.12.029
- Marinescu, P. J., Levin, E. J., Collins, D., Kreidenweis, S. M., & van den Heever, S. C. (2019). Quantifying aerosol size distributions and their temporal variability in the southern great plains, USA. Atmospheric Chemistry and Physics, 19(18), 11985–12006. https://doi.org/10.5194/acp-19-11985-2019
- Marshak, A., Ackerman, A., da Silva, A. M., Eck, T., Holben, B., Kahn, R., et al. (2021). Aerosol properties in cloudy environments from remote sensing observations: A review of the current state of knowledge. *Bulletin America Meteorology Social*, 102(11), E2177–E2197. https://doi. org/10.1175/BAMS-D-20-0225.1
- Marshak, A. & Davis, A. (Eds.) (2025). 3D radiative transfer in cloudy atmospheres (p. 2005). Springer Science & Business Media.
- Marshak, A., Platnick, S., Várnai, T., Wen, G., & Cahalan, R. F. (2006). Impact of three-dimensional radiative effects on satellite retrievals of cloud droplet sizes. *Journal of Geophysical Research*, 111(D9), D09207. https://doi.org/10.1029/2005jd006686
- Monteith, J. L., & Unsworth, M. H. (2013). Chapter 2 Properties of gases and liquids. In J. L. Monteith & M. H. Unsworth (Eds.), Principles of environmental physics (4th ed., pp. 5–23). Academic Press.
- Newsom, R., Goldsmith, J., & Sivaraman, C. (2017). Raman lidar MERGE value-added product. In DOE office of science atmospheric radiation measurement (ARM) program.
- Newsom, R., & Sivaraman, C. (2018). Raman lidar water vapor mixing ratio and temperature value-added products. In DOE office of science atmospheric radiation measurement (ARM) program.
- Newsom, R. K., Bambha, R., & Chand, D. (2022). Raman lidar (RL) instrument handbook. In DOE office of science atmospheric radiation measurement (ARM) program.
- NOAA Air Resources Laboratory. (2024). HYSPLIT model [Software]. Retrieved from https://www.ready.noaa.gov/HYSPLIT\_traj.php
- Painemal, D., Chiu, J. Y. C., Minnis, P., Yost, C., Zhou, X., Cadeddu, M., et al. (2017). Aerosol and cloud microphysics covariability in the northeast Pacific boundary layer estimated with ship-based and satellite remote sensing observations. *Journal of Geophysical Research: At-mospheres*, 122(4), 2403–2418. https://doi.org/10.1002/2016JD025771

HU ET AL. 17 of 18

- Parworth, C., Fast, J., Mei, F., Shippert, T., Sivaraman, C., Tilp, A., et al. (2015). Long-term measurements of submicrometer aerosol chemistry at the southern great plains (SGP) using an aerosol chemical speciation monitor (ACSM). *Atmospheric Environment*, 106, 43–55. https://doi.org/10.1016/j.atmosenv.2015.01.060
- Pöschl, U. (2005). Atmospheric aerosols: Composition, transformation, climate and health effects. Angewandte Chemie International Edition, 44(46), 7520–7540. https://doi.org/10.1002/anie.200501122
- Prather, K. A., Hatch, C. D., & Grassian, V. H. (2008). Analysis of atmospheric aerosols. Annual Review of Analytical Chemistry, 1, 485–514. https://doi.org/10.1146/annurev.anchem.1.031207.113030
- Reilly, P. J., & Wood, R. H. (1969). Prediction of the properties of mixed electrolytes from measurements on common ion mixtures. *The Journal of Physical Chemistry*, 73(12), 4292–4297. https://doi.org/10.1021/j100846a043
- Riemer, N., West, M., Zaveri, R., & Easter, R. (2010). Estimating black carbon aging time-scales with a particle-resolved aerosol model. *Journal of Aerosol Science*, 41(1), 143–158. https://doi.org/10.1016/j.jaerosci.2009.08.009
- Ritsche, M. (2011). ARM surface meteorology systems instrument handbook. DOE/SC-ARM/TR-086. In DOE office of science atmospheric radiation measurement (ARM) program.
- Rosenfeld, D., Lohmann, U., Raga, G. B., O'Dowd, C. D., Kulmala, M., Fuzzi, S., et al. (2008). Flood or drought: How do aerosols affect precipitation? *Science*, 321(5894), 1309–1313. https://doi.org/10.1126/science.1160606
- Sicard, M., Fortunato Dos Santos Oliveira, D. C., Muñoz-Porcar, C., Gil-Díaz, C., Comerón, A., Rodríguez-Gómez, A., & Dios Otín, F. (2022). Measurement report: Spectral and statistical analysis of aerosol hygroscopic growth from multi-wavelength lidar measurements in Barcelona, Spain. Atmospheric Chemistry and Physics, 22(11), 7681–7697. https://doi.org/10.5194/acp-22-7681-2022
- Singh, A., & Kuang, C. (2024). Scanning mobility particle sizer (SMPS) instrument handbook. DOE/SC-ARM-TR-147. U.S. Department of Energy, Atmospheric Radiation Measurement user facility.
- Spänkuch, D., Hellmuth, O., & Görsdorf, U. (2022). What is a cloud? Toward a more precise definition. *Bulletin America Meteorology Social*, 103(8), E1894–E1929. https://doi.org/10.1175/BAMS-D-21-0032.1
- Su, T., Li, Z., Roldán, N., Luan, Q., & Yu, F. (2024). Constraining effects of aerosol-cloud interaction by accounting for coupling between cloud and land surface. *Science Advances*, 10(21), eadl5044. https://doi.org/10.1126/sciadv.adl5044
- Su, T., Zheng, Y., & Li, Z. (2022). Methodology to determine the coupling of continental clouds with surface and boundary layer height under cloudy conditions from lidar and meteorological data. *Atmospheric Chemistry and Physics*, 22(2), 1453–1466. https://doi.org/10.5194/acp-22-1453-2022
- Tackett, J. L., & Di Girolamo, L. (2009). Enhanced aerosol backscatter adjacent to tropical trade wind clouds revealed by satellite-based lidar. Geophysical Research Letters, 36(14), L14804. https://doi.org/10.1029/2009gl039264
- Thorsen, T. J., & Fu, Q. (2015). Automated retrieval of cloud and aerosol properties from the ARM raman lidar. Part II: Extinction. *Journal of Atmospheric and Oceanic Technology*, 32(11), 1999–2023. https://doi.org/10.1175/JTECH-D-14-00178.1
- Thorsen, T. J., Fu, Q., Newsom, R. K., Turner, D. D., & Comstock, J. M. (2015). Automated retrieval of cloud and aerosol properties from the ARM Raman lidar. Part I: Feature detection. *Journal of Atmospheric and Oceanic Technology*, 32(11), 1977–1998. https://doi.org/10.1175/ JTECH-D-14-00150.1
- Titos, G., Jefferson, A., Sheridan, P. J., Andrews, E., Lyamani, H., Alados-Arboledas, L., & Ogren, J. A. (2014). Aerosol light-scattering enhancement due to water uptake during the TCAP campaign. *Atmospheric Chemistry and Physics*, 14(13), 7031–7043. https://doi.org/10.5194/acp-14-7031-2014
- Trishchenko, A. P., Luo, Y., Latifovic, R., & Li, Z. (2004). Land cover type distribution over the ARM SGP area for atmospheric radiation and environmental research. In Fourteenth atmospheric radiation measurement science team meeting. US Dep. of Energy.
- Twohy, C. H., Coakley, J. A. Jr., & Tahnk, W. R. (2009). Effect of changes in relative humidity on aerosol scattering near clouds. *Journal of Geophysical Research*, 114(D5), D05205. https://doi.org/10.1029/2008jd010991
- Uin, J. (2016). 3002 humidified tandem differential mobility analyzer (HTDMA) instrument handbook. DOE/SC-ARM-TR-161. In DOE office of science atmospheric radiation measurement (ARM) program.
- Uin, J., Cromwell, E., Hayes, C., & Salwen, C. (2021). Humidified tandem differential mobility analyzer (AOSHTDMA), southern great plains (SGP), Lamont, OK (extended and Co-located with C1) (E13) [Dataset]. Atmospheric Radiation Measurement (ARM) User Facility. https://doi.org/10.5439/1776643
- Várnai, T., & Marshak, A. (2002). Observations of three-dimensional radiative effects that influence MODIS cloud optical thickness retrievals. Journal of the Atmospheric Sciences, 59(9), 1607–1618. https://doi.org/10.1175/1520-0469(2002)059<1607:ootdre>2.0.co;2
- Várnai, T., & Marshak, A. (2011). Global CALIPSO observations of aerosol changes near clouds. Geoscience and Remote Sensing Letters, 8(1), 19–23. https://doi.org/10.1109/LGRS.2010.2049982
- Wang, J., Collins, D., Covert, D., Elleman, R., Ferrare, R. A., Gasparini, R., et al. (2006). Temporal variation of aerosol properties at a rural continental site and study of aerosol evolution through growth law analysis. *Journal of Geophysical Research*, 111(D18), D18203. https://doi. org/10.1029/2005jd006704
- Wang, Y., Bagya Ramesh, C., Giangrande, S. E., Fast, J., Gong, X., Zhang, J., et al. (2023). Examining the vertical heterogeneity of aerosols over the southern great plains. *Atmospheric Chemistry and Physics*, 23(24), 15671–15691. https://doi.org/10.5194/acp-23-15671-2023
- Wang, Y., Li, Z., Zhang, Y., Du, W., Zhang, F., Tan, H., et al. (2018). Characterization of aerosol hygroscopicity, mixing state, and CCN activity at a suburban site in the central north China plain. Atmospheric Chemistry and Physics, 18(16), 11739–11752. https://doi.org/10.5194/acp18-11739-2018
- Watson, T. B. (2017). Aerosol chemical speciation monitor (ACSM) instrument handbook. DOE/SC-ARM-TR-196. In DOE office of science atmospheric radiation measurement (ARM) program.
- Wen, G., Marshak, A., & Cahalan, R. F. (2006). Impact of 3-D clouds on clear-sky reflectance and aerosol retrieval in a biomass burning region of Brazil. *IEEE Geoscience and Remote Sensing Letters*, 3(1), 169–172. https://doi.org/10.1109/lgrs.2005.86138
- Wu, X., Balmes, K. A., & Fu, Q. (2021). Aerosol direct radiative effects at the ARM SGP and TWP sites: Clear skies. *Journal of Geophysical Research: Atmospheres*, 126(5), e2020JD033663. https://doi.org/10.1029/2020jd033663
- Yang, C. K., Chiu, J. C., Marshak, A., Feingold, G., Várnai, T., Wen, G., et al. (2022). Near-cloud aerosol retrieval using machine learning techniques, and implied direct radiative effects. Geophysical Research Letters, 49(20), e2022GL098274. https://doi.org/10.1029/2022gl098274
- Zawadowicz, M., Howie, J., Shilling, J., & Levin, M. (2021). ACSM, corrected for composition-dependent collection efficiency (ACSMCDCE), southern great plains (SGP), Lamont, OK (extended and co-located with C1) (E13) [Dataset]. Atmospheric Radiation Measurement (ARM) User Facility. https://doi.org/10.5439/1763029
- Zhang, S. L., Ma, N., Kecorius, S., Wang, P. C., Hu, M., Wang, Z. B., et al. (2016). Mixing state of atmospheric particles over the North China Plain. Atmospheric Environment, 125, 152–164. https://doi.org/10.1016/j.atmosenv.2015.10.0532022

HU ET AL. 18 of 18